the end-points of the NEB calculations and the corresponding energies are used as the references when calculating Li diffusion activation barriers. Based on the NEB calculation results, when Li ions diffuse between two equilibrium sites, they prefer a curved diffusion path that avoids the empty A sites (Figure 6.3(a)). The crosses in Figure 6.2(a) are the saddle points in the calculated minimum energy paths for Li diffusion. The obtained energy barriers are 230meV (from Li1 to Li2) and 22meV (from Li2 to Li3), which is much lower than the previous values reported by Catti et al.[137]. The discrepancy may be from the following possible reasons: firstly, our predicted pathway is different, which was obtained by NEB method instead of the "Frozen Ion" method adopted by previous work. NEB has been proved to be pretty reliable on predicting the pathways and finding minimum energy path on the potential energy surface. Secondly, different DFT functionals were used. However, we believe the U correction is not playing a role. Besides the data showed in this work, we have also calculated the pathway and diffusion barriers without U correction, which gives us consistent results.

6.1.3.1.2 High lithium concentration scenario

The same method used in calculations of the low lithium concentration model is adopted for the high lithium concentration scenario $Li_{0.35}La_{0.55}TiO_3$. In all cases, space group P1 is used to reduce the symmetry constrains to a minimum. It is a supercell composed of $\sqrt{5}a_p \times \sqrt{5}a_p \times 4a_p$. The 2D cell in (001) plane is composed of five A-sites occupied by Li, La or vacancies. Three different models are established with different in-plane cation arrangements and the layer stacking sequences. Similar to the low lithium concentration model, La-rich and La-poor layers are alternatively arranged; in addition, because of La ion's large radii and its strong interactions with Li ions, the principle of as

less La in the Li layer as possible is adopted in this model. The calculated energies are listed in Table 6.1. Due to the structure complexity, our investigations are focused on the La-poor layer (z=1/8, 4Li + 1 □) of model I, which is the lowest in energy among the proposed models, drawn in Figure 6.1(d). This model can be rationalized that by having the least number of La in the La-poor layer helps reducing the repulsion forces and results in the lowest energy. The corresponding 2D cell of the La poor layer (z=1/8) is shown in Figure 1(e) and the structure of this layer after relaxation is depicted in Figure 6.1(f). After structural relaxation, Li equilibrium sites are also close to the center of vertical oxygen square window, similar to the results obtained in the low lithium concentration scenario. NEB calculations are performed to find the diffusion paths and energy barrier for the circled Li. A similar curved diffusion path can be found as shown in Figure 6.3(b). The minimum energy path avoids both the empty A-site and the three other Li ions. The highest activation barrier for this diffusion path is around 390meV, and there also are barriers in other local environments around 120meV within this path.

6.1.3.2 Experimental Results

6.1.3.2.1 Materials Characterization: SEM/EDS, XRD and TEM

The morphology of pristine and LLTO coated powders were examined by scanning electron microscopy (SEM) (Figure 6.4(a-d)). The pristine particles have a very uniform size distribution of around 100 nm. The primary particle size after the LLTO coating is slightly increased ranging between 100-200 nm. It is hypothesized that some sintering of primary particles may have occurred during the LLTO coating process, as

can be seen in the SEM images. From Figure 6.5 (a), the XRD data of pristine, 1wt% LLTO coated (LLT1), 2wt% LLTO coated (LLT2) and 5wt% LLTO coated (LLT5) samples shows that the main peaks are representative of the layered structure $LiNi_{0.8}Co_{0.15}Al_{0.05}O_2$ with the $R\bar{3}m$ symmetry group; in addition, the existence of doublets at (006)/(102) and (108)/(110) indicates the well-layered structure with little Li/Ni interlayer mixing. In Figure 6.5 (b) and (c), the most intense peaks are associated with the LLTO phase [145] of 2θ=24.6°, 31.6°, 33.6° and appear for all three coated samples. All three peaks, however, shifted to a lower angle as compared to the published data on the bulk of LLTO, [145] which indicates larger interplane distances in the LLTO coating. Figure 6.4(e-g) show respectively the EDS results of pristine, LLT1 and LLT5, which represents that the amount of La and Ti elements increases with the coating weight percentage.

To further investigate the surface morphology of pristine and coated materials, TEM images were taken. The surface coating is mostly like small islands distributed on the surface of pristine material (inset in Fig 6.4(c), the while spots indicates the coating material). In addition, some particles were coated uniformly. The inset in Figure 6.4(d) depicts clearly the interface between the core material and the coating material.

6.1.3.2.2 Electrochemical property test

The electrochemical property testing of the pristine and coated electrodes were performed to examine the coating effect on cyclic performance, and rate capability. Figure 6.6(a) displays the discharge capacity retention with cut-off voltage 4.4V. As shown in the figure, materials with LLTO coating (1wt%, 2wt%, 5wt%) maintained at least 99% capacity (compared to 1st discharge) after ten cycles, while the pristine material

only retained around 85% of 1st cycle discharge capacity after ten cycles. In this work, LLT1 was adopted as the representative sample for further in-depth investigation on the role of the LLTO coating material on the NCA electrodes.

Figure 6.6(b) and (c) show the rate testing data for pristine and LLT1 electrodes at the rate of C/20 for charging and C/20, C/10, C/5, C/2, 1C, 2C for discharging, in the voltage range of 4.4-2.0V. All the cells for rate testing are with a loading density of around 5mg/cm^2. As can be seen from the graph, the capacity at C/20 has been improved from around 125mAh/g to 135mAh/g; the improvement of the coated samples is most obvious at higher rates of C/2, 1C and 2C. For C/2, 1C and 2C, the capacities for the pristine electrode are 82mAh/g, 68mAh/g, and 44mAh/g, respectively. On the other hand, the LLT1 electrode shows much higher capacity, 105mAh/g, 93mAh/g, and 82mAh/g. In addition, the OCV drop for the pristine material at the beginning of each discharge is more severe at the higher rates. In the case of the 2C rate, the cell voltage of the pristine electrode drops to 3.45V, while the LLT1 electrode remains at 4.0V.

In order to further identify the reasons for the improved rate capability of the LLT1 electrode, a PITT test was performed, and Li chemical diffusion coefficients in both pristine and LLT1 coated electrodes are extracted. The results were obtained from a step size of 10mV and current limit corresponding to a C/200 rate. The linearity of ln (I) vs. t is good enough for the analysis shown below. A semi-logarithmic plot of the current vs. time was extracted based on the long-time dependence, $\tau >> L^2/\widetilde{D}_{Li}$. The lithium diffusion can be solved with Fick's law for a semi-infinite system with a perturbation of the surface concentration in Eq. 1 [146]

$$I(t) = \frac{2Fa\ (C_s - C_0)\widetilde{D}}{L} \exp(-\frac{\pi^2 \widetilde{D}}{4L^2} t)$$

The lithium chemical diffusion coefficient was obtained from the slope of the linearity of ln (*I*) vs. t in Eq. 2

$$\widetilde{D} = -\frac{dln(I)}{dt} \cdot \frac{4L^2}{\pi^2}$$

Figure 6.7 (a) plots the calculated lithium diffusion coefficient ($\widetilde{D}_{LiLi}$) vs. the state of charge. The LLTO coating increases the chemical lithium diffusion coefficient by almost one order of magnitude at any state of charge (except for the voltage 3.7-3.8V) compared to that of the pristine electrode. Another interesting fact is that the valley of the diffusion coefficient profile moves from 3.65V for the pristine electrode to 3.75V for the LLT1 electrode. The valley in the diffusion coefficient plot is generally representative of a two-phase reaction, the value of which is usually two to three magnitudes of orders lower than the diffusion coefficient in the single-phase region. [37] There has also been a study on the two-phase reaction during the first charge of this material; and the valley is associated with the fact that another hexagonal phase would appear and coexist with the original hexagonal phase. [38] In general, the LLTO coating layer delays the occurrence of a two-phase reaction by 0.1V.

EIS measurements were carried out to study the effects of the LLTO coating on the interfacial characteristics between the electrolyte and the active materials. Figures 6.7 (b) and (c) exhibit the impedance spectra of the active materials from the three-electrode cell configuration at a cell potential of 4.2V. The impedance spectra consist of two semicircles in the high and intermediate frequency range and a line inclined in the low frequency. The two semicircles at the high and intermediate frequency are attributed to

Li^+ ion transport through the SEI and interfacial charge-transfer reaction combined with electrochemical double-layer capacitive behavior, respectively. The latter inclined line is responsible for the solid-state lithium diffusion into the active material. For the quantitative analysis, the simplified equivalent circuits presented in the insets of Figure 6.7 (b) and (c) were used. The values of all electrical parameters were taken from the CNLS (Complex non-linear least square) fitting method to the equivalent circuits, as summarized in Table 6.1.

As listed in Table 6.1, all reaction resistances in LLT1 electrode have relatively smaller numbers than those in the pristine electrode. The resistances of SEI films, R_f, interfacial charge transfer reactions, R_{ct}, and Warburg coefficient A_w which is due to the solid-state lithium diffusion in the active material, decreased by 64%, 84%, and 52%, respectively. This indicates that every elementary reaction step at the interface is considerably improved by the LLTO coating layer. In the very low-frequency (<10mHz), however, the impedance behavior of LLT1 electrode is found to be different from that of the pristine electrode. (The data are not presented in this work.) The LLT1 impedance spectra have an additional semicircle at very low frequency. One possibility is that another charge transfer reaction happens at the interface between LLTO coating and the NCA active material since there is a change in the local structures from LLTO to NCA. [147] Further investigation will be carried out to identify the charge transfer mechanism.

6.1.3.2.3 STEM_EELS mapping results

STEM images as well as EELS mapping were performed to examine the existence of coating before and after cycling. The RGB composite mapping is depicted in Figure

6.8. Signals for Ti and La elements can be clearly seen from the EELS map. It indicates that the coating will not get detached from the surface during cycling therefore has a lasting effect after cycling.

6.1.4 Discussions

In this study, first principles calculations are performed to characterize LLTO, one of the solid electrolyte candidates, fast lithium ion conductors. The fast lithium conductivity is supported by our first principles calculation results. In the low lithium concentration scenario, even the highest activation barrier of Li in-plane diffusion is as low as 230 meV, which is much lower than the typical calculated Li diffusion barriers in layered compounds such as NCA. [148] For the high lithium concentration scenario, the highest barrier is around 390 meV. Such discrepancy between the two models, however, is probably caused by the different numbers of vacancies in the same plane for the migrating Li ion. In our calculations, due to the size limitation of the model supercells, the barriers in the high lithium concentration model were calculated with only one vacancy adjacent to the migrating Li ion, while in low lithium concentration model, two vacancies were located besides the migrating Li ion. As suggested by previous study, the rate of non-perfect crystals is very sensitive to the density of discrete vacancy sources. [43] Moreover, note that the relatively high diffusion barrier is reached only in a specific local environment, and barriers in other local environments can be as low as 22meV. Since all computations are performed at 0K, Li, La ions and vacancies are arranged in a highly

ordered way. At room temperature, such site ordering is much reduced and the overall lithium diffusion activation energies should be lowered.[144]

This solid electrolyte candidate, LLTO, has been applied as a coating material to our NCA cathode material in lithium ion half-cells. SEM, EDS, TEM and XRD results consistently suggest that the coating material LLTO exists on the surface of the NCA material and it is crystalline in nature. Nevertheless, the shift of the XRD peaks for our samples of LLTO indicates larger interplane distances and therefore possible local structure change of the perovskite LLTO.

As shown in Figure 6.6(a), the cycling performances of coated samples are significantly improved, which is consistent with previous study on a different layered oxide.[149] Such improvement is generally attributed to the surface protection of the coating. For high voltage cathode materials such as NCA, the high operating voltage may cause the decomposition of the $LiPF_6$ salt, generating HF in the electrolyte. For uncoated samples, the electrode surface is in directly contact with the electrolyte, thus the active materials might be dissolved into the electrolyte due to the HF etching.[150,151] Meanwhile, the electrode surface which is unstable at high voltage undergoes structural reconstruction and forms a spinel-like phase near the surface. This phenomenon is suggested by the large OCV drop at the beginning of each discharge for the uncoated sample in this study. The LLTO coating existed on the electrode surface prevents the NCA materials from direct contact with the electrolyte, therefore can largely reduce the dissolution of active materials and suppress the surface structural change at high voltage. The capacity retention of the LLTO coated samples is significantly improved as a result.

Besides the cycling performance, the rate capability of coated sample is also enhanced as indicated in Figure 6.6 (b) and (c). The high ionic conductivity of the LLTO coating materials is regarded as a key factor affecting the rate performance. Although the introduction of a coating layer creates another interface between the active material and the coating material, which may add an extra resistance to Li transportation, it is compensated by the fast lithium transportation inside the coating layer and the suppression of SEI formation. The overall impedance therefore is reduced significantly in the coated sample. As obtained from PITT results, the Li chemical diffusion coefficient in LLTO coated sample is one order of magnitude higher than that of the uncoated sample. The EIS results also show that the SEI layer impedance of the coated sample is much lower. For the LLT1 sample, the impedance for Li^+ diffusion in the SEI layer is even lowered by more than 60%. These observations suggest that the enhancement of the solid-state lithium diffusion caused by the LLTO coating should be an important contribution factor to the improved rate capability. This kinetic process may be an explanation for the delay of two-phase (the valley) in PITT results. Furthermore, the whole impedance for the active material is reduced for LLTO coated electrode compared to the pristine electrode; this may be another reason for the higher voltage where two-phase reaction occurs.

Lastly, we note that the coating material would not decompose or detach from the NCA active material after cycling (cut-off voltage 4.2V) by STEM/EELS. It indicates that the coating has a lasting effect. A further study of LLTO coating will be carried out on other high voltage cathode materials, such as high voltage cathodes (cut off voltage

4.6-4.8V), to see whether the LLTO coating will continue to play a role in other higher voltage systems.

6.1.5 Conclusions

In summary, we demonstrated the significant improvement on rate capabilities and capacity retention on layered cathode material NCA by applying a fast ionic conduction solid electrolyte coating. We elucidate the mechanism of the solid electrolyte LLTO coating with a joint study of experiment and computation. LLTO has *intrinsically high* ionic conductivity. Therefore, besides acting as a protective coating layer, it reduces the impedance of Li^+ diffusion in the composite electrode, as well as the impedances of interfacial charge transfer and transportation through the SEI layer. In addition, the coating layer is relatively stable after cycling resulting in a continuous effect upon cycling. Our findings shed some new light on applying solid electrolyte as coating in high voltage cathode materials and understanding the mechanism of coating in lithium ion batteries. The stability of the LLTO coating material upon longer cycling, higher voltage exposure (> 4.5V) and higher temperature exposure, remains to be examined.

6.2 AlF_3 coating for lithium-ion battery cathodes

6.2.1 Introduction

The common idea of surface modification is to reduce potential side reactions, such as HF etching and the formation of undesirable products within the solid-electrolyte

interface film (SEI), between electrode and electrolyte at high working voltage[152]. Based upon published works during the past few years, there are several different surface modification strategies applied to Li-excess. The most widely used surface modification materials are oxides, fluorides, and phosphates, for example, TiO_2, Al_2O_3, AlF_3, and $AlPO_4$; [153-155] however, most of these materials are electron and ion insulators. Learning from the case of $LiFePO_4$, carbon and Al has been used as a coating layer on Li-excess, in order to improve the electronic conductivity of the material.[156,157] Other researchers have introduced an ionic conductor to the surface of Li-excess, such as, lithium phosphorus oxynitride (LiPON), $LiNiPO_4$, and Li_3VO_4.[158-161] Manthiram et al. combined the advantages of different surface modifications and developed hybrid strategies. One of their recent works combined reduced graphene oxide and $AlPO_4$, which largely suppressed undesired SEI formation.[162] In contrast to the studies mentioned above, Thackeray et. al. showed a slightly mild acid treatment will also reduce the first cycle irreversible capacity loss of Li-excess layered oxides.[163]

Although these surface modifcations improved the electrochemical performance of Li-excess, the fundemental role in terms of their chemical and structural effects, are still not well understood. In this work, we prepared Li-excess layered oxide with composition of $Li_{1.2}Ni_{0.2}Mn_{0.6}O_2$ (LNMO) through a routine hydroxide co-precipitation method. A mild acid NH_4F and metal precipitant Al^{3+} were used together to modify the surface of Li-excess. By synthesizing an Al_2O_3 surface coating via incorporation of NH_4F, the electrochemical performance of Li-excess was markedly improved. Aberration corrected transmission electron microscopy (a-STEM) / electron energy loss spectroscopy (EELS) was carried out to investigate the chemical and structural changes

after surface co-modification, enabling us to explain how the NH_4F and Al_2O_3 surface co-modification improved the initial coulombic efficiency, rate capability, and cycling stability of Li-excess. These findings will guide us in designing reasonable surface modifications in the future.

6.2.2 Methodologies

6.2.2.1 TEM

TEM images were collected using an FEI Tecnai G2 Polara cryoelectron microscope with a field emission gun and a voltage of 300 kV. The powders were suspended on a 300-mesh copper grid with lacey carbon.

6.2.2.2 *a*-STEM/EELS

Electron microscopy work was carried out on a Cs corrected FEI Titan 80/300-kV TEM/STEM microscope equipped with a Gatan Image Filter Quantum-865. All STEM images and EELS spectra were acquired at 300 KV and with a beam size of ~0.7 Å. EELS spectra shown in this work were acquired from a square area of ~0.5 ×0.5 nm using an acquisition time of 2 s and a collection angle of 35 mrad. High angle annular dark field (HAADF) images were obtained at a convergence angle of 30 mrad and a large inner collection angle of 65 mrad. Images acquired by an HAADF detector with a small convergence angle and a relatively large inner collection angle are also called "Z-contrast" images, where the contrast is proportional to $Z^{1.7}$.[114,115] Atomic resolution Z-contrast images can be used to differentiate elements and provide atomic−structural information based on the contrast of the atomic columns.

To minimize possible electron beam irradiation effects, EELS and HAADF figures presented in this work were acquired from areas without pre-beam irradiation. Mn L_3 to L_2 intensity ratio analysis was performed using the method described by Wang et al.[95]

6.2.3 Results and Discussions

High-resolution transmission electron microscopy was used to identify the Al_2O_3 coating on surface modified material. Figure 6.9 a and b are the HRTEM images of pristine (LNMO) and treated (NALNMO), respectively. The TEM images of both materials show very good layered crystal structure. Amorphous films are observed on the surface of NALNMO, while the LNMO shows a very clean surface. More than 20 particles were analyzed to examine the amorphous film. As shown in Figure 6.9 b, this amorphous film is unevenly coated on the surface, with thickness ranging from 0 nm to 2.5 nm. As our recent study indicates, the surface chemistry of LNMO varies with different preparation methods.[164] We apply the same NH_4F and Al_2O_3 surface co-modification on LNMO prepared by carbonate method, which forms uniform Al_2O_3 coating with a thickness of 1 nm as showed. In addition to the amorphous coating, there are small islands sitting on the surface of particles, as illustrated in Figure 6.9 c, which are not observed in our pristine $Li_{1.2}Ni_{0.2}Mn_{0.6}O_2$. Figure 6.9 d depicts the TEM image of these small islands at higher magnification. The island exhibits a well-layered crystal structure and particle size around 20 nm. EELS was performed on the islands to verify that it is active material instead of Al-related compounds.

Figure 6.10 depicts the differences between the bulk and surface structure of NALNMO. Multiple grains were selected for study and the results were consistent;

therefore, only representative data are shown here. The diffraction pattern of the FFT represented by the blue squared region at the surface with a "spinel-like" structure compared to the red-squared region in the bulk. After NH_4F and Al_2O_3 surface co-modification, there is a 3 nm “spinel-like” phase on the bulk, layered phase.

In addition to direct visualization of the crystal structure changes, EELS was carried out to obtain chemical information. Two representative particles were observed and studied. One is the R-3m (-101) zone axis particle as the inset electron diffraction pattern of Figure 6.11 a showed, the other is R-3m (010) zone axis particle which is presented in Figure 6.11 d. EELS was performed on NALNMO from bulk to surface, with step size of ~1 nm, as showed in Figure 6.11 a and d. The L_3 and L_2 edges of transition metals are due to the electronic excitation from the $2p^{3/2}$ to $3d^{3/2}$ and $3d^{5/2}$ orbitals and from the $2p^{1/2}$ to $3d^{3/2}$ orbital, respectively. Previous studies have shown that the L_3/L_2 ratio is sensitive to the valence state of Mn.[165,166] The L_3/L_2 ratio plotted as a function of distance from surface to bulk in Figure 6.11 b and e. The L_3/L_2 edge ratios of both particles reveal that the Mn valence remains 4+ in the bulk, as it does in pristine LNMO[167]. However, the (-101) zone axis particle (Figure 6.11 d) shows Mn valence reduced to 3+ within a 3 nm region of the surface. The corresponding O K-edge of bulk and surface are plotted in red and purple, respectively. The pre-peak in O K-edge is due to the transition of 1s electrons to the unoccupied 2p orbitals, which hybridize with the TM 3d orbitals. The decrease in the pre-peak in the (-101) zone axis particle agrees with the reduction of Mn at the surface.[168]

6.2.4 Conclusions

The use of a-STEM/ EELS enabled us to understand the structural and chemical aspects of the materials studied from both bulk and surface perspectives. The complex changes on the material's surface after NH_4F and Al_2O_3 surface co-modification included the formation of "spinel-like" phase, the etched island active material, an amorphous Al_2O_3 coating, and the reduction of surface Mn. After the modification, the first cycle coulombic efficiency, the rate capacity and cycling capacity was improved. These understandings will guide us in designing better cathode materials for lithium ion batteries of the future.

Chapter 6, Part 1, in full, is a reprint of the material "Lithium lanthanum titanium oxides: a fast ionic conductive coating for lithium-ion battery cathodes", Chemistry of Materials, 2012, 24(14), 2744, by Danna Qian, B. Xu, H. -M. Cho, T. Hatsukade, K. J. Carroll, Y. S. Meng, Copyright (2012) American Chemical Society. The dissertation author is the primary investigator and author of the material. Part2, in part, is a reprint of the material "Understanding the role of NH_4^+ and Al_2O_3 surface co-modification on lithium-excess layered oxide $Li_{1.2}Ni_{0.2}Mn_{0.6}O_2$" submitted. The dissertation author is the primary investigator and author.

Figures:

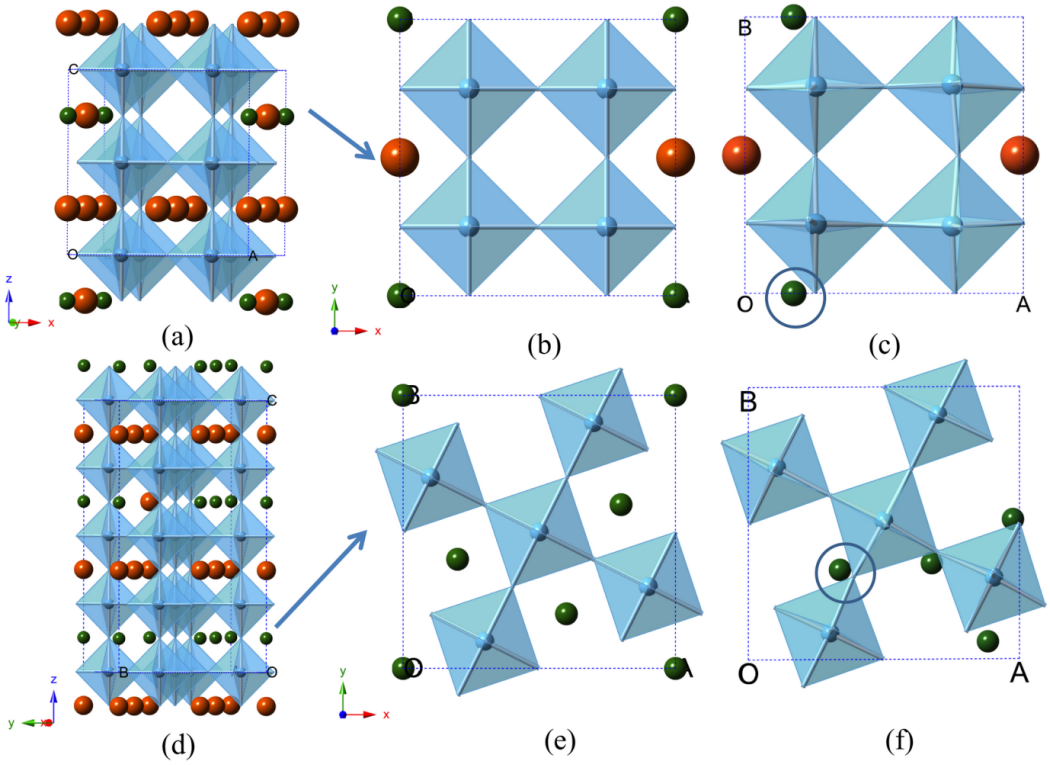

Figure 6.1: Computational model structure of $Li_{0.125}La_{0.625}TiO_3$(a) and $Li_{0.35}La_{0.55}TiO_3$ (d). Planes of interest used in NEB calculation of low lithium concentration (b) and high lithium concentration (e). (c) and (f) are the after relaxation structure of planes in (b) and (e) respectively.

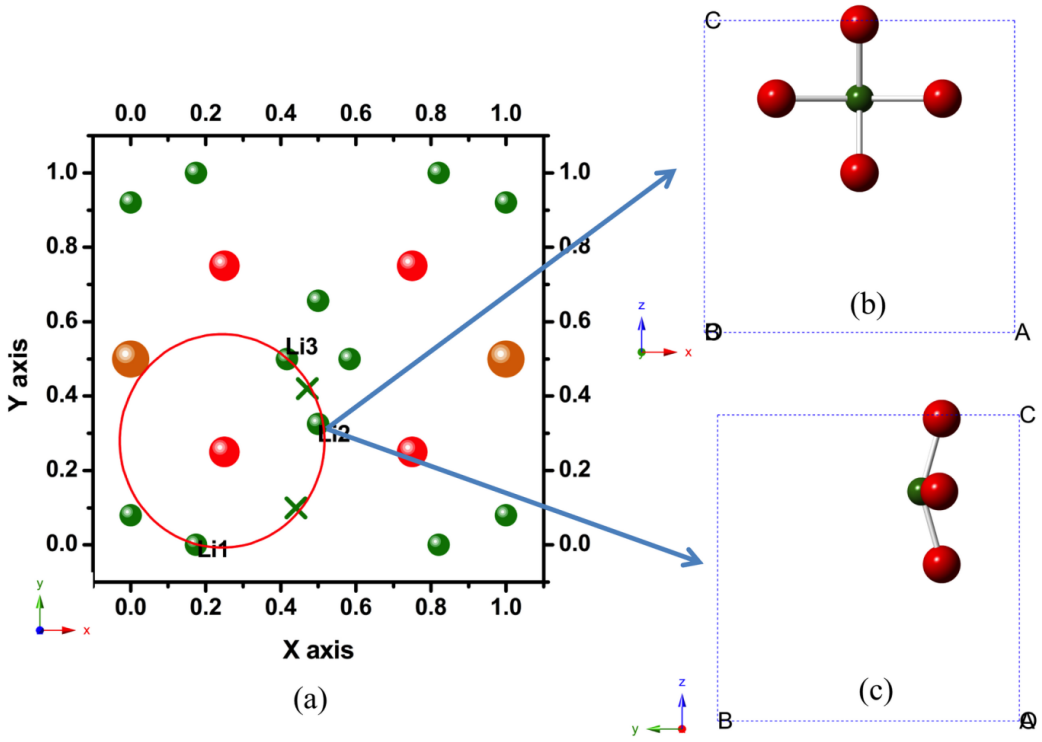

Figure 6.2: (a) x=3/4 plane of low lithium concentration with all equilibrium states and middle images. Two crosses are the images between Li1 and Li2, Li2 and Li3 respectively. (Other images can get from symmetry). (b) (c) Illustration of vertical oxygen square window from different view directions.

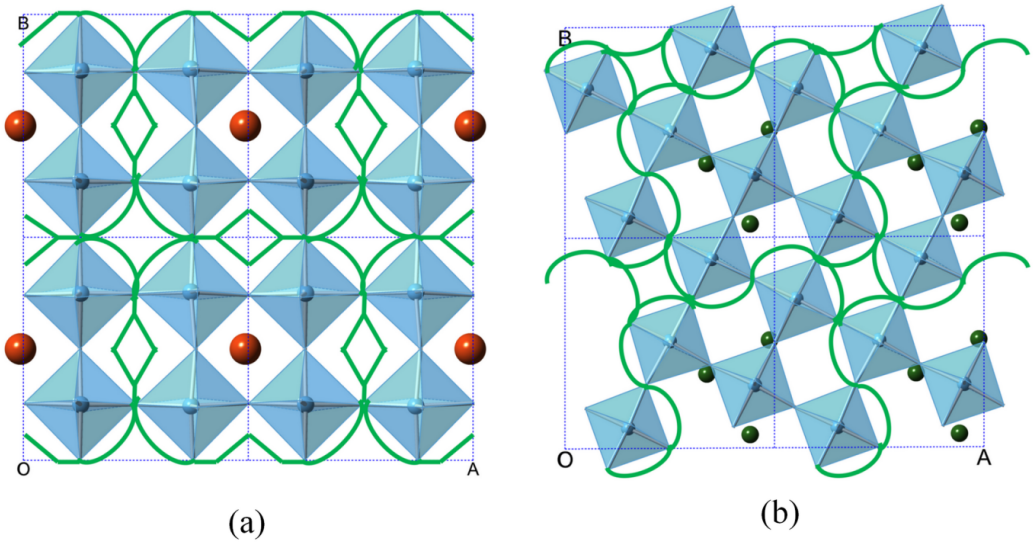

Figure 6.3: Estimated Li diffusion path in La-poor layer (green dash lines) in low lithium concentration scenario (a) and high lithium concentration scenario (b)

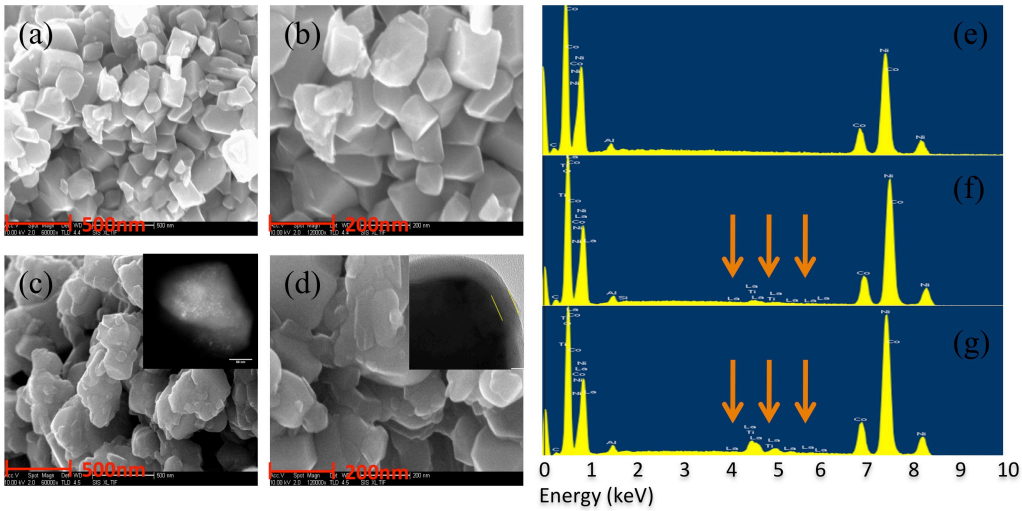

Figure 6.4: Structural characterization of pristine and LLTO coated samples. (a) (b) and (c)(d) are the SEM images of pristine and LLT5, respectively; (e) (f) and (g) are EDS results of pristine, LLT1 and LLT5, respectively. The inset in (c) and (d) is the TEM image of LLT5.

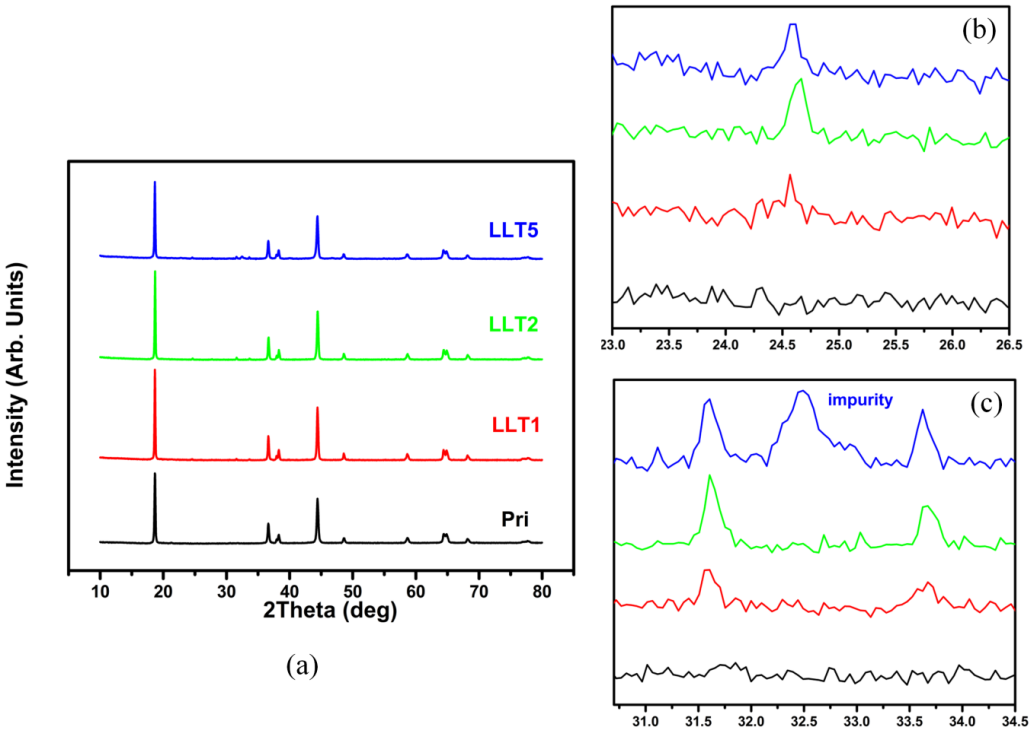

Figure 6.5: (a) XRD results of pristine, LLT1, LLT2, and LLT5. (b) Zoom in of 23° ~ 26.5°. (c) Zoom in of 30.5° ~ 34.5°.

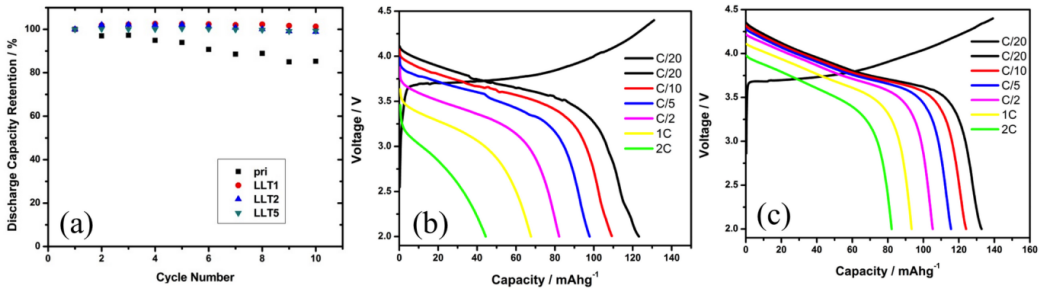

Figure 6.6: Electrochemical cycling and rate capability of pristine and coated electrodes. (a) Cycling retention properties of pristine, LLT1, LLT2 and LLT5. Rate capability of pristine (b) and LLT1 (c).

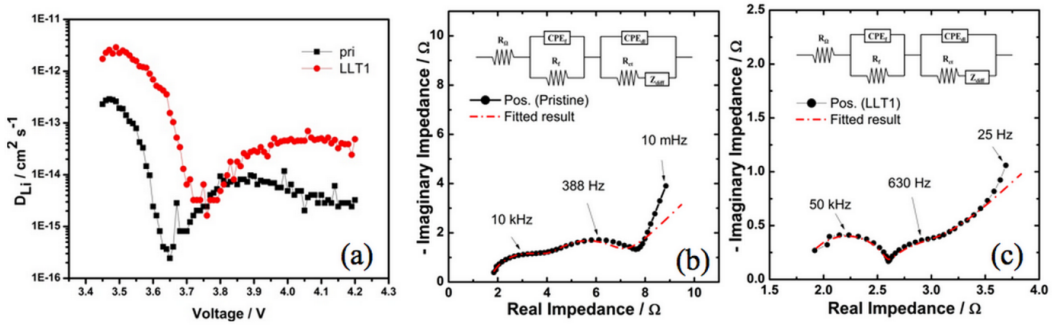

Figure 6.7: (a) Calculated Li ion diffusion coefficient of pristine (black) and LLT1 (red) from PITT tests. Impedance spectra (100kHz – 100mHz) of pristine (b) and LLT1 (c) obtained from the cell at 4.2V. The insets are the equivalent circuit model used to fit the experimental model. Dashed lines are the CNLS fittings of the impedance spectra of the equivalent circuit model.

(a) (b)

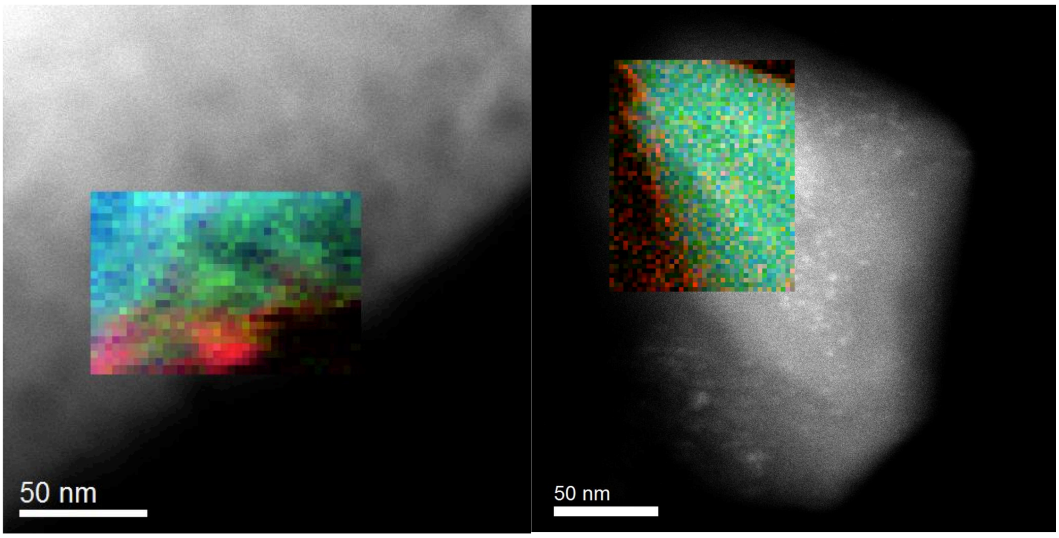

Figure 6.8: EELS mapping of LLT5 (a) before and (b) after cycling. Green: Li; Blue: La; Red: Ti

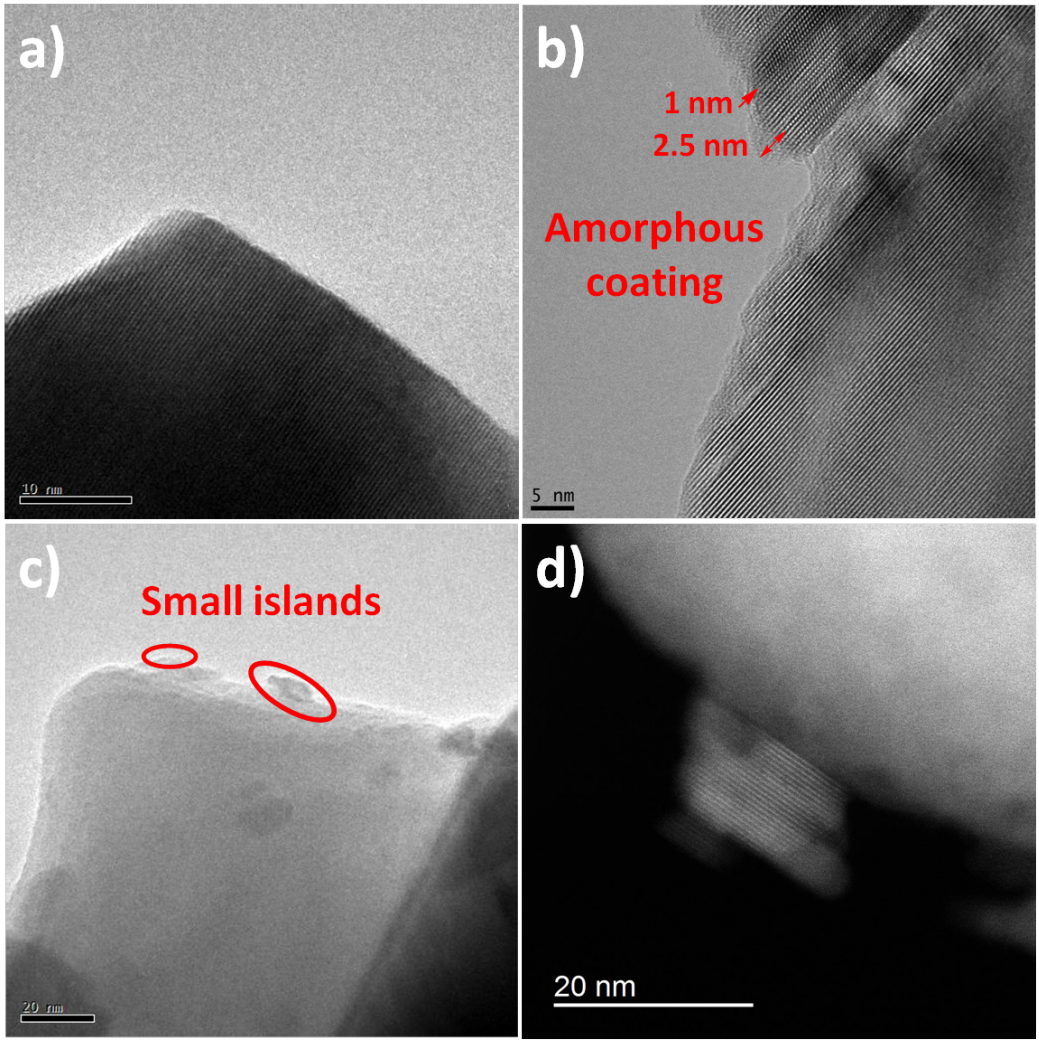

Figure 6.9: The TEM and STEM of LNMO and NALNMO, a) TEM of LNMO, b) and c) TEM of NALNMO, d) STEM of NALNMO.